nature communications

Article

https://doi.org/10.1038/s41467-026-77664-0

Nonlinear spectral modeling and control of soft-robotic muscles from data

Received: 16 December 2025

Accepted: 25 August 2026

Published online: 16 September 2026

Check for updates

Leonardo Bettini [1,3], Amirhossein Kazemipour [2,3], Robert K. Katzschmann [2] ✉ & George Haller [1] ✉

Artificial muscles are essential for compliant musculoskeletal robotics but complicate control due to nonlinear multiphysics dynamics. Electrohydraulic actuators, a class of soft artificial muscles, offer high performance but exhibit memory effects and hysteresis. Here we present a data-driven reduction and control strategy grounded in spectral submanifold theory. In the adiabatic regime, where inputs vary slowly relative to intrinsic transients, trajectories rapidly converge to a low-dimensional slow manifold. We learn an explicit input-to-output map on this manifold directly from forced-response trajectories, eliminating the need for decay experiments generated by large step inputs, which can induce pronounced hysteretic behavior and are often unrepresentative of normal operating conditions. We deploy the spectral-submanifold-based model for real-time control of an antagonistic electrohydraulic-clutch joint. This approach yields a substantial reduction in tracking error compared to feedback-only and feedforward-only baselines under identical settings. This record-and-control workflow enables rapid characterization and high-performance control of soft muscles and muscle-driven joints without detailed physics-based modeling.

The adaptability, compliance, and efficiency of biological systems increasingly inspire advances in robotics. In musculoskeletal systems like the human arm, rigid elements (bones) provide structure and transmit forces, while soft components (muscles, ligaments, tendons) connect and actuate them, enabling fine control and safe interaction with delicate environments. Soft elements prevent damage from rigid contact, ensuring compliance. Soft-material-based robots extend these advantages, offering flexibility, adaptability, and compatibility with complex geometries, particularly valuable in human-interactive applications such as surgical tools and prosthetics[1–3]. Artificial muscles, emulating biological force generation, are key to innovations in musculoskeletal robotics and assistive technologies[4,5].

Despite these benefits, modeling and control of soft artificial muscles remain challenging, primarily due to the complex interplay among soft materials, electrostatic forces, fluidic dynamics, and frictional contacts. These effects lead to memory, hysteresis, and other nonlinearities that complicate analysis and real-time control[3,6]. Reduced-order models (ROMs) are therefore attractive, as they capture essential dynamics with minimal equations while balancing interpretability and efficiency (see refs. 7,8 for recent reviews). In practice, artificial muscles operate within larger assemblies and are affected by fabrication imperfections such as partial adhesion or misalignment, which add uncertainty. Under these conditions, analytic ROMs become limited and hard to scale, motivating a shift toward data-driven modeling that captures system dynamics directly from data without precise parameter identification[3,6].

Among data-driven modeling techniques, the recently developed spectral submanifold (SSM) reduction has addressed similar challenges across various physical systems[9]. SSM reduction preserves the essential nonlinear dynamics of high-dimensional systems in a compact and interpretable form. Specifically, slow SSMs are low-dimensional, smooth, and attracting invariant manifolds in the phase space, emerging from the system's slowest linear modes[10]. Trajectories near the SSM quickly converge onto it and evolve according to its internal

[1]Institute for Mechanical Systems, ETH Zurich, Zurich, Switzerland. [2]Soft Robotics Lab, ETH Zurich, Zurich, Switzerland. [3]These authors contributed equally: Leonardo Bettini, Amirhossein Kazemipour. ✉e-mail: rkk@ethz.ch; georgehaller@ethz.ch

dynamics, yielding accurate and robust nonlinear reduced-order models. SSM reduction has proven effective in both equation-based and purely data-driven settings[9], accurately capturing nonlinear decay in free responses and predicting forced responses under periodic and quasiperiodic excitations[11–16].

Recent theoretical advances have extended SSM theory to nonlinear systems under temporally aperiodic excitations[9,17], broadening its applicability to practical engineering fields such as robotics. The extended theory accommodates time-dependent inputs that are either moderate in amplitude or vary slowly relative to the system's internal time scales of the uncontrolled system. The latter setting case is known as the adiabatic setting. Building on promising simulation results in soft-robot control via SSM theory[18], Alora et al.[19] demonstrated an experimental implementation using a leading-order approximation of an adiabatic SSM (aSSM) anchored at the origin, achieving both computational and data efficiency. However, this approach assumes trajectories remain near the origin, limiting its scope. This restriction was recently lifted by Kaundinya et al.[20], who developed a data-driven aSSM reduction and control strategy for a finite-element model of a soft trunk robot.

In this work, we also focus on the adiabatic setting, where intrinsic dynamics evolve much faster than external forcing. We further consider the regime in which this timescale separation is strong enough to justify neglecting the internal dynamics on the adiabatic spectral submanifold (aSSM), focusing instead on the slow manifold (SM) to which the aSSM is anchored. This is a fair approximation for soft artificial muscles, whose internal actuation and material transients are typically strongly damped and decay rapidly relative to the motion along a desired trajectory. Crucially, the learned SM admits a fast inverse map, enabling real-time feedforward control that can be combined with feedback for accurate trajectory tracking in antagonistic muscle configurations.

Experimental evidence of pronounced time-scale separation in soft-robotic systems comes, for example, from Hydraulically Amplified Self-Healing Electrostatic (HASEL) actuators, which are also the focus of this work. HASELs are part of the broader class of electrohydraulic artificial muscles, offering a compelling alternative to motor-driven systems by overcoming the bulkiness, rigidity, and limited compliance of electromagnetic motors[21–27]. These designs are inspired by animal musculoskeletal architecture, where bones, tendons, and contractile actuators work together for efficient, compliant motion[28–31]. HASEL actuators combine soft fluidic and electrostatic actuation to achieve compliant yet powerful contraction in lightweight, scalable structures. They consist of oil-filled polymer pouches partially coated with electrodes; applying voltage deforms the pouch, redistributing the dielectric liquid and generating contraction. Extension occurs passively under external loads or via antagonistic actuation in multi-muscle assemblies[32], enabling bidirectional motion, variable stiffness, and rapid disturbance rejection. The fast electrostatic and fluidic transients relative to the slower mechanical response produce the slow-fast dynamics of the adiabatic regime, making HASELs an ideal platform for the SM-based modeling introduced here.

Kellaris et al.[33] proposed a quasi-static model for HASEL actuators, wherein the actuator stroke, parametrized by a single degree of freedom, is obtained by minimizing the system's free energy to find equilibrium. Originally developed for electrostatic zipping actuators[34–36], this approach links static deformation to applied voltage through an analytical relationship depending on physical parameters like initial pouch angle, film thickness, actuator width, undeformed pouch length, and dielectric permittivity, requiring precise measurements for accuracy. Later studies highlighted modeling's role in closed-loop control. Johnson et al.[37] identified the input-output relationship via frequency response testing, enabling frequency-domain controller design. Yeh et al.[38] developed a three-dimensional dynamical model using the Port-Hamiltonian formalism. Like the quasi-static model, these approaches depend on detailed physical parameter identification, illustrating the trade-off between interpretability and the practical challenges of measuring precise system properties.

These studies, however, focus on isolated HASEL actuators, which are rarely used alone. In practice, HASELs are embedded in complex assemblies. For example, Kazemipour et al.[32] enhanced a robotic arm's range of motion by integrating HASELs with electrostatic clutches. These thin, flexible electroadhesive elements modulate shear adhesion via a low-current voltage signal, rapidly switching between a high-holding-force state (to transmit muscle force) and a low-friction state (to release the opposing tendon), thereby enabling bidirectional joint motion and variable stiffness without tendon slack. Precise control of such antagonistic systems requires accurate, computationally efficient models. Continuum models are too slow for real-time use, while black-box approaches lack reliability. Multi-physics coupling and switching dynamics introduce nonlinearities and hysteresis that resist analytical treatment, motivating data-driven reduced-order modeling: learning system dynamics directly from experiments while remaining computationally efficient. In this context, our SM-based, data-driven method provides a scalable, interpretable approach for predicting and controlling multi-actuator HASEL systems, inherently accounting for component interactions and fabrication imperfections.

In this work, we introduce a methodology for performing SM reduction directly from experimental data and demonstrate its use for real-time control of antagonistic artificial muscles. As outlined in Fig. 1c and Supplementary Video 1, the procedure is detailed in Sections "Model reduction to spectral submanifolds" and "Adiabatic spectral submanifold and slow manifold", applied to numerical examples in Section "Illustration of data-driven aSSM and SM modeling on analytic models", and validated on experimental data in Section "Data-driven modeling of experimental artificial muscles". Section "SSM-enabled closed-loop control of an antagonistic joint" presents closed-loop control experiments on an antagonistic musculoskeletal joint with HASEL actuators and electrostatic clutches. We compare three strategies, PI feedback only, inverse-SSM feedforward only, and their combination ("Methods" subsection "Control design and implementation"), showing that the combined controller achieves substantially lower tracking errors. On randomized test trajectories under identical saturation and slew-rate limits, the inverse-SSM+PI controller (RMS error of 2.38°, max 10.41°) outperforms the baselines, i.e., feedforward-only (RMS error of 3.63°, max 16.67°) and PI-only (RMS error of 7.63°, max 26.00°). These results confirm that data-driven slow-manifold models not only predict system behavior accurately but also enable high-performance, real-time control of complex antagonistic muscle systems, bridging the gap between theoretical model reduction and practical robotic applications. To the best of our knowledge, this represents the first experimental demonstration of spectral submanifold theory applied to closed-loop control of antagonistic soft robotic systems with quantified performance improvements over standard control baselines.

Results

We first present the theoretical and data-driven reduction method (SSM, aSSM, and SM), validate it on analytic models and on experimental HASEL actuators, and then demonstrate closed-loop control on an antagonistic joint. Together, these results show that a simple inverse map learned on the slow manifold yields accurate predictions and real-time control on hardware.

Model reduction to spectral submanifolds

Consider an autonomous dynamical system of the form

$$\dot{\boldsymbol{x}} = \boldsymbol{f}(\boldsymbol{x}) = \boldsymbol{A}\boldsymbol{x} + \boldsymbol{f}_0(\boldsymbol{x}), \qquad \begin{aligned} &\boldsymbol{x} \in \mathbb{R}^n, \quad \boldsymbol{A} \in \mathbb{R}^{n\times n}, \\ &\boldsymbol{f}_0 \in \mathcal{C}^r, \quad \boldsymbol{f}_0 = \mathcal{O}(|\boldsymbol{x}|^2), \end{aligned} \tag{1}$$

https://doi.org/10.1038/s41467-026-77664-0

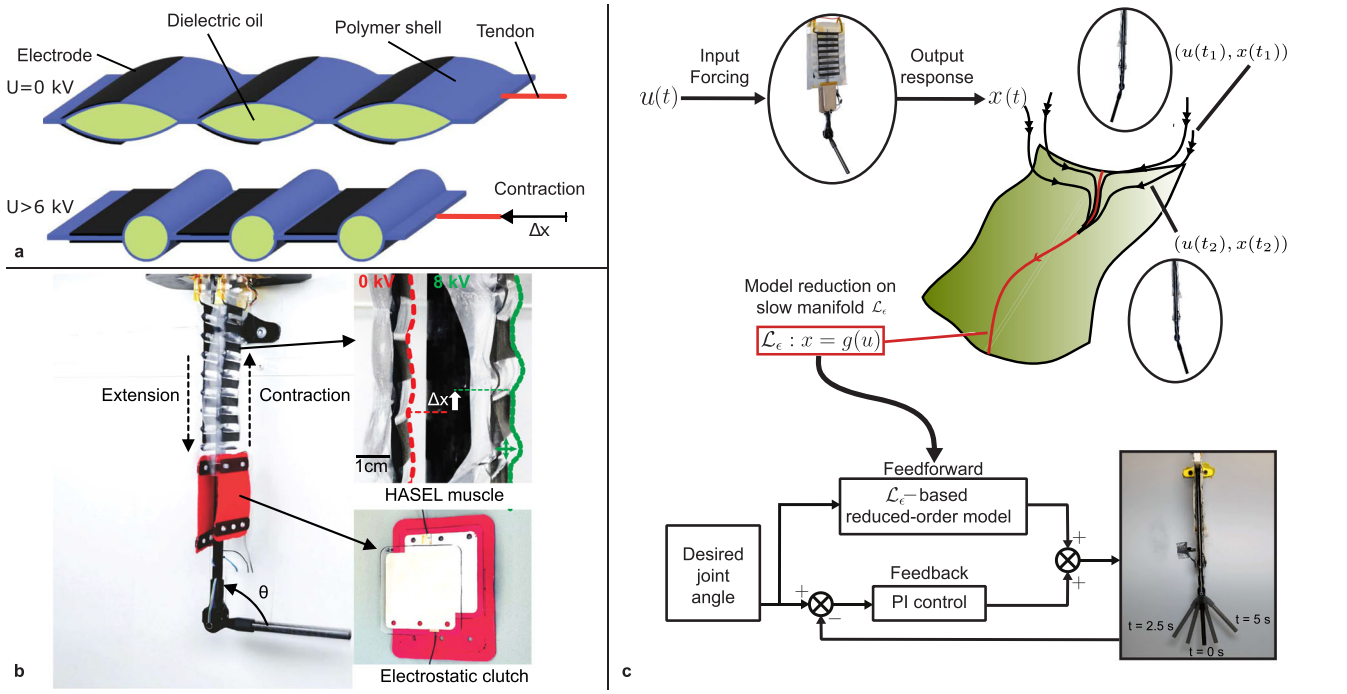


Fig. 1 | Overview of data-driven slow manifold modeling and control for antagonistic artificial muscles. a HASEL actuator working principle: a flexible polymer shell filled with dielectric oil and covered by electrodes; applying voltage (up to $U = 8$ kV) generates electrostatic pressure that redistributes the fluid, producing axial contraction Δx against a tendon load. **b** Experimental platform: antagonistic musculoskeletal joint actuated by HASEL artificial muscles paired with electrostatic clutches, enabling bidirectional motion and variable stiffness; θ denotes the joint angle. The inset shows the contraction Δx at 0 kV and 8 kV. Reproduced from ref. 32. Copyright 2026 Author(s), licensed under a Creative Commons Attribution (CC BY) license. **c** Data-driven modeling and control: pronounced time-scale separation allows trajectories to rapidly converge onto a low-dimensional slow manifold $\mathcal{L}_\epsilon$, learned directly from forced-response trajectories. The learned polynomial map $x = g(u)$ relates control input $u(t)$ to system state $x(t)$. The inverse slow-manifold model provides feedforward control, combined with proportional-integral (PI) feedback for disturbance rejection.

for some integer $r \geq 1$, where $\boldsymbol{f}_0(\boldsymbol{x})$ represents the nonlinear part and $\boldsymbol{f}_0(0) = \boldsymbol{0}$, so that the system has a fixed point at the origin. We assume the fixed point to be linearly asymptotically stable, i.e.,

$$\mathrm{Re}\lambda_n \leq \mathrm{Re}\lambda_{n-1} \leq \cdots \leq \mathrm{Re}\lambda_2 \leq \lambda_1 < 0. \tag{2}$$

Each distinct eigenvalue λ_j of the linear part $\boldsymbol{A}$ is associated with a real eigenspace E_j, which is spanned by the real and imaginary parts of the eigenvector or generalized eigenvectors corresponding to λ_j. A slow spectral subspace E is defined as the direct sum of a group of ℓ eigenspaces corresponding to the ℓ slowest eigenvalues in Eq. (2)

$$E = E_1 \oplus E_2 \oplus \cdots \oplus E_\ell. \tag{3}$$

As discussed in Haller and Ponsioen[10], eigenspaces and spectral subspaces admit unique smoothest nonlinear continuations under generically satisfied nonresonance conditions of the spectrum of $\boldsymbol{A}$. These continuations are referred to as primary SSMs and denoted as $\mathcal{W}(E)$. The primary SSM attracts all nearby trajectories in the phase space exponentially, and hence its internal dynamics serve as an ideal nonlinear reduced-order model of the full system.

Adiabatic spectral submanifold and slow manifold

Let us now reconsider system (1) under time-dependent forcing $\boldsymbol{u}(t) \in \mathbb{R}^f$ in the form

$$\begin{aligned} \dot{\boldsymbol{x}} &= \boldsymbol{A}\boldsymbol{x} + \boldsymbol{f}_0(\boldsymbol{x}) + \boldsymbol{f}_1(\boldsymbol{x}, \boldsymbol{u}), \quad \boldsymbol{f}_1 \in \mathcal{C}^r, \\ \dot{\boldsymbol{u}} &= \epsilon \boldsymbol{w}(\boldsymbol{x}, \epsilon t), \qquad 0 \leq \epsilon \ll 1, \end{aligned} \tag{4}$$

where ϵ characterizes the order of the rate of change of the external forcing. For $0 \leq \epsilon \ll 1$, $\boldsymbol{u}(t)$ evolves on a slower timescale than the system's intrinsic dynamics, placing the system in the adiabatic regime, as defined by Haller and Kaundinya[17]. In control applications, the term $\boldsymbol{f}_1$ represents the external input applied to the system, with its additive contribution to the autonomous dynamics justified in the Supplementary Material. This input depends both on the system state, through a feedback law, and on time, to follow a desired trajectory. The adiabatic assumption is particularly well suited to robotics, where the internal dynamics of the system (e.g., actuator response) are significantly faster than the evolution of the controlled motion. This separation of time scales enables the system to rapidly synchronize with the control input and track complex trajectories with high accuracy and responsiveness.

For $\epsilon = 0$, the external forcing becomes constant and acts as a fixed parameter of the system. As seen in Fig. 2a, for each fixed value of $\boldsymbol{u}$, the system dynamics evolve toward a unique attracting fixed point along a corresponding slow SSM, $\mathcal{W}(E(\bar{u}))$. The set of these fixed points forms an invariant manifold denoted by $\mathcal{L}_0$, which is a critical manifold in the terminology of geometric singular perturbation theory (see Feniche[39]). The union of SSMs taken over all values of $\boldsymbol{u}$ defines a higher-dimensional invariant manifold $\mathcal{M}_0$, which globally attracts nearby trajectories.

For $\epsilon > 0$, the external forcing varies slowly in time, as shown in Fig. 2b, c. In this regime, the critical manifold $\mathcal{L}_0$ perturbs into a slow manifold (SM), $\mathcal{L}_\epsilon$, and the invariant manifold $\mathcal{M}_0$ perturbs into the adiabatic SSM (aSSM) denoted by $\mathcal{M}_\epsilon$. This manifold $\mathcal{M}_\epsilon$ remains attracting and smoothly varies with the slow forcing. Its internal dynamics capture the essential, low-dimensional behavior of the full system, thereby serving as an accurate reduced-order model. Importantly, this reduced-order model can be learned directly from data, as we discuss in the "Methods" subsection "Data-driven modeling via adiabatic spectral submanifolds".

https://doi.org/10.1038/s41467-026-77664-0

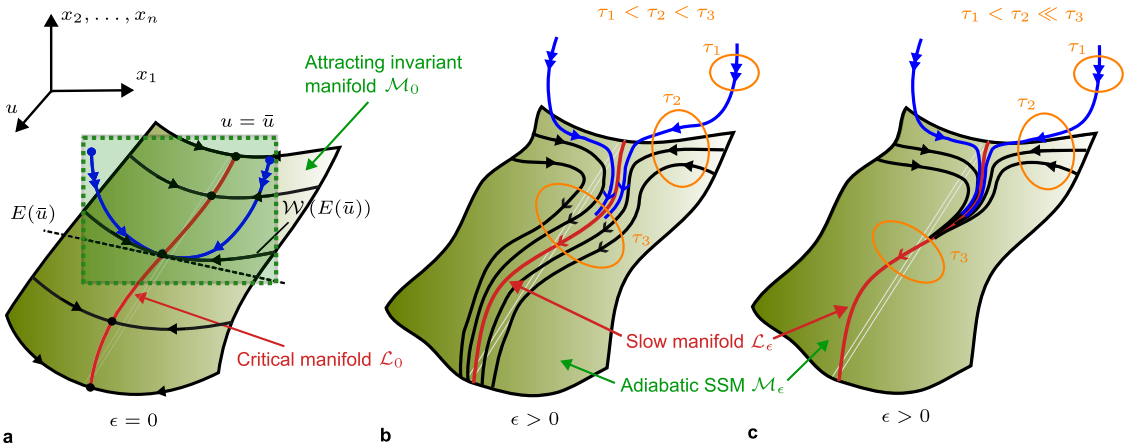


Fig. 2 | Adiabatic spectral submanifolds and slow-manifold reduction across time scales. a Geometry of the attracting invariant manifold $\mathcal{M}_0$ formed by a family of SSMs, $\mathcal{W}(E(u))$, parametrized by the external forcing parameter u, for $\epsilon = 0$. For simplicity, u is assumed to be a scalar in this plot. The critical manifold $\mathcal{L}_0$ consists of the collection of the fixed points corresponding to each value of u. **b** For $\epsilon \neq 0$, the manifold $\mathcal{M}_0$ perturbs into an aSSM, $\mathcal{M}_\epsilon$, and $\mathcal{L}_0$ perturbs into a slow manifold, $\mathcal{L}_\epsilon$. The dynamics of the external forcing is associated with the hollow arrowhead. **c** Trajectories rapidly converge to $\mathcal{L}_\epsilon$ when the timescales τ_1 and τ_2 of the autonomous dynamics are much faster than the timescale τ_3 of the external excitation. In all panels, black curves indicate trajectories on the invariant manifolds, blue curves indicate trajectories converging to them.

In this adiabatic setting, we identify three well-separated time scales:

- a fast time scale τ_1, associated with transient dynamics that lie outside the aSSM, $\mathcal{M}_\epsilon$;
- an intermediate time scale τ_2, governing the dynamics confined to the aSSM, $\mathcal{M}_\epsilon$;
- a slow time scale τ_3, determined by the rate of change of the external forcing, which also dictates the evolution on the slow manifold $\mathcal{L}_\epsilon$ to which $\mathcal{M}_\epsilon$ is attached.

These three time scales satisfy the hierarchy $\tau_1 < \tau_2 < \tau_3$, as schematically illustrated in Fig. 2. Experimental observations of HASEL actuators and HASEL-based artificial muscles confirm this time scale hierarchy: the system dynamics exhibit rapid convergence to the aSSM, $\mathcal{M}_\epsilon$, followed by a slower alignment with the slow manifold, $\mathcal{L}_\epsilon$. Physically, this implies that internal transients decay much more rapidly than the evolution along the desired trajectory, i.e., $\tau_1 < \tau_2 \ll \tau_3$, as seen in Fig. 2c. As a result, modeling the dynamics solely on the slow manifold provides an accurate and computationally efficient representation of the dominant dynamics of the system (see "Methods" subsection "Data-driven modeling via slow manifold"), without resolving fast transients. Hence, the SM reduction offers a pragmatic solution for control, as the faster aSSM dynamics contribute only marginally to the performance.

We now introduce the non-dimensional metric ρ to quantify the slowness of a control input signal $\boldsymbol{u}(t)$ (associated with the time scale τ_3) relative to the autonomous decay $\boldsymbol{x}(t)$ (associated with τ_1 and τ_2), motivated by similar quantities defined in Haller and Kaundinya[17] and Kaundinya et al.[20]. We assume that a scalar observable $s(t)$ characterizes the autonomous system response and $\gamma(t)$ the response under external forcing $u(t)$. For a control application, $\gamma(t)$ would be the desired path. The observable $s(t)$ is shifted, if necessary, to vanish at the $x = 0$ origin. We further normalize $s(t)$ as:

$$\tilde{s}(t) = \frac{s(t)}{\left(\int_0^\infty |s(t)|^2 dt\right)^{1/2}} \tag{5}$$

and $\gamma(t)$ as:

$$\tilde{\gamma}(t) = \frac{\gamma(t)}{\left(\int_{t_i}^{t_f} |\gamma(t)|^2 dt\right)^{1/2}}, \tag{6}$$

where the forced signal is considered in the time interval $[t_i, t_f]$. We define the dimensionless slowness measure

$$\rho = \frac{\left(\int_{t_i}^{t_f} |\dot{\tilde{\gamma}}(t)|^2 dt\right)^{1/2}}{\left(\int_0^\infty |\dot{\tilde{s}}(t)|^2 dt\right)^{1/2}}. \tag{7}$$

For instance, for a linear autonomous system with observed displacement $s(t) = s_0 e^{\lambda t}$ and $\lambda < 0$, ρ simplifies to

$$\rho = \frac{\left(\int_{t_i}^{t_f} |\dot{\tilde{\gamma}}(t)|^2 dt\right)^{1/2}}{|\lambda|}. \tag{8}$$

In that case, the condition $\rho \ll 1$ ensures that the forced dynamics evolve slowly relative to the intrinsic decay of the system, thereby justifying the reduction to the slow manifold (see Fig. 2c). Figure 3 intuitively illustrates the meaning of the metric ρ in a regulation task, comparing slow and fast control actions to the system's autonomous transient decay. In general, we expect the slow-manifold reduction to remain valid for $\rho < 1$, with the quality of the approximation improving as ρ becomes increasingly smaller than one.

In the following, we adopt the normalized mean trajectory error (NMTE) from Cenedese et al.[11] as a measure of the average deviation between the predicted and actual trajectories to assess the accuracy of the model. The NMTE is defined as:

$$\text{NMTE} = \frac{1}{\|\boldsymbol{x}\|} \frac{1}{N} \sum_{j=1}^{N} \|\boldsymbol{x}_j - \hat{\boldsymbol{x}}_j\|, \tag{9}$$

where $\boldsymbol{x}$ denotes the true data, $\hat{\boldsymbol{x}}$ the corresponding model prediction, and N the total number of temporal observations.

https://doi.org/10.1038/s41467-026-77664-0

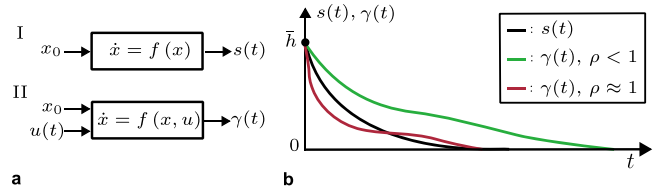


Fig. 3 | Slowness measure compares controlled and autonomous transient dynamics. a Autonomous system (I) and externally forced system (II). **b** Comparison of trajectories decaying to zero from the same initial point $\bar{h}$ through autonomous transient decay and under slower ($\rho < 1$) and faster ($\rho \approx 1$) control in a regulation task.

Illustration of data-driven aSSM and SM modeling on analytic models

We first illustrate the power of aSSM-reduced modeling on data generated by analytic HASEL actuator models.

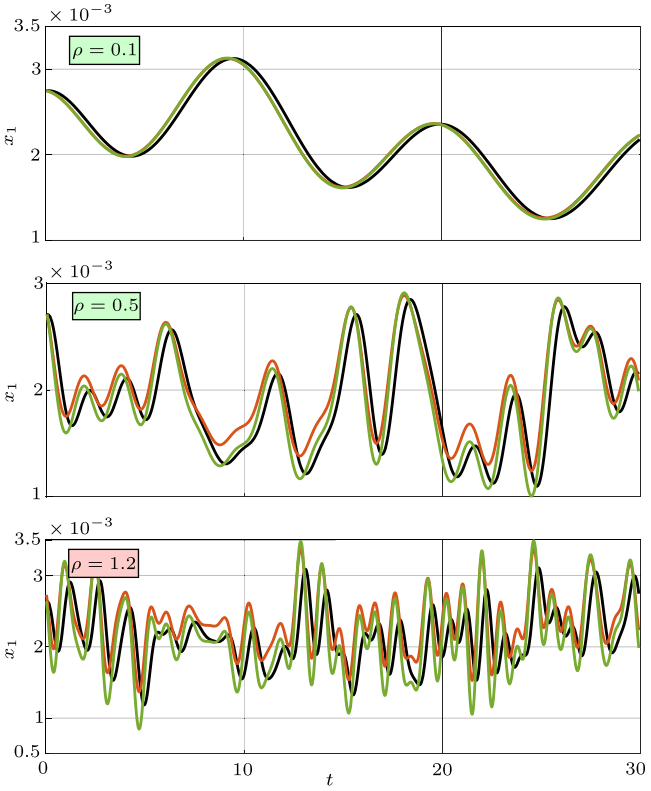
Simple phenomenological model of HASEL actuator: we consider a single-degree-of-freedom nonlinear oscillator that captures the qualitative behavior of HASEL actuators under voltage-driven excitation. This oscillator model is of the nondimensional form

$$m\ddot{x} + c(u)\dot{x} + kx + \alpha x^3 = \gamma u^2(t), \tag{10}$$

with $c(u) = \tilde{c} - \beta u^2$ and with $u(t)$ representing the externally applied voltage. The term proportional to β introduces a voltage-dependent damping mechanism, allowing the input to modulate the system's effective relaxation time. Although the relationship between damping and voltage may be nonlinear and non-monotonic in experimental systems, the present model is designed to capture the potential influence of the input on internal decay rates. The term proportional to γ acts as a purely external forcing input. To reproduce the overdamped behavior observed in experimental HASEL actuators, we set the model parameters to $m = 0.022$, $k = 1$, $\tilde{c} = 0.3$, $\alpha = 0.7$, $\beta = 5 \cdot 10^{-3}$, and $\gamma = 0.5$.

This example aims to illustrate how the rate of external forcing affects the predictive performance of reduced-order models (in this case, one-dimensional) based on the aSSM and the SM approximation. We employ a leading-order approximation of the aSSM, as outlined in the "Methods" subsection "Data-driven modeling via adiabatic spectral submanifolds". The aSSM is constructed by collecting decaying trajectories at fixed voltage levels. For each fixed input, the system converges to a locally attracting SSM, from which the reduced dynamics and parametrization are learned. These local SSMs are then interpolated across voltage values to approximate the aSSM, $\mathcal{M}_\epsilon$ and its internal dynamics under slowly varying forcing. As a simplification of this procedure, the SM approach directly infers the input-state relationship from forced trajectories, without requiring decay experiments. This method assumes that internal dynamics decay sufficiently fast for the system state to remain close to a low-dimensional manifold defined instantaneously by the input.

Figure 4 compares the responses predicted by the aSSM and SM models under random voltage forcing. Although in general the SM is defined by a nonlinear function of the input, a linear approximation suffices in this simple example. We consider two cases with different forcing rates. For the fast forcing case ($\rho = 0.5$), the correction introduced by the leading-order aSSM significantly improves prediction accuracy. In contrast, as reported in Fig. 4b, when the forcing varies more slowly ($\rho = 0.1$), the system remains close to the SM, and the SM model yields sufficiently accurate predictions. Finally, for faster forcing ($\rho = 1.2$), both the SM- and aSSM-based predictions lose accuracy, as expected. Although such a high value of ρ would be uncommon in practice, it illustrates the necessity of a time scale separation in the mathematical results underpinning aSSM reduction. We also emphasize that only the leading-order approximation of both the



ρ	$\text{NMTE}_{\text{aSSM}}$ [%]	NMTE_{SM} [%]
0.1	1.7	1.7
0.5	6.3	6.6
1.2	12.6	12.0

Fig. 4 | Model accuracy depends on the external forcing rate. a Comparison between the aSSM-based and the SM-based reduced-order model of the SDOF of Eq. (10) under random external excitations with increasing speed ($\rho = 0.1$ (top), $\rho = 0.5$ (middle) and $\rho = 1.2$ (bottom)). As predicted by theory, the slow manifold approximation is accurate when $\rho \ll 1$, while in the last case, even the leading-order aSSM-based approximation breaks down. **b** Legend and table reporting the Normalized Mean Trajectory Error (NMTE) values for the different cases.

parametrization and the reduced dynamics of the aSSM is used here. Higher-order approximations derived by Haller and Kaundinya[17] would further enhance accuracy but would also require more data in order to avoid an overfit.

Analytical model of the HASEL actuator from the literature: we now extend the simple model (10) of the HASEL actuator by incorporating the pouch geometry shown in Fig. 5a. This extension couples the deflection angle α of the pouch with the generated stroke x, and explicitly models the electrostatic forces acting on the electrodes. The pouches are treated as two-dimensional, assuming negligible influence from the out-of-plane depth. The actuator geometry follows the configuration presented in Kellaris et al.[33]. While we adopt a Lagrangian approach to derive the governing equations, these are equivalent to those obtained via the Port-Hamiltonian formalism[40,41] employed by Yeh et al.[38]. Further details on the derivation are provided in the Supplementary Material.

The actuator consists of N pouches connected in series. Each pouch is formed by bonding two rectangular dielectric films, each of length L_p, width w, and thickness t, along their edges. Within the experimental parameter range of interest, the dielectric films can be modeled as inextensible membranes without bending stiffness. Under these assumptions, the liquid-filled pouch adopts a cross-sectional

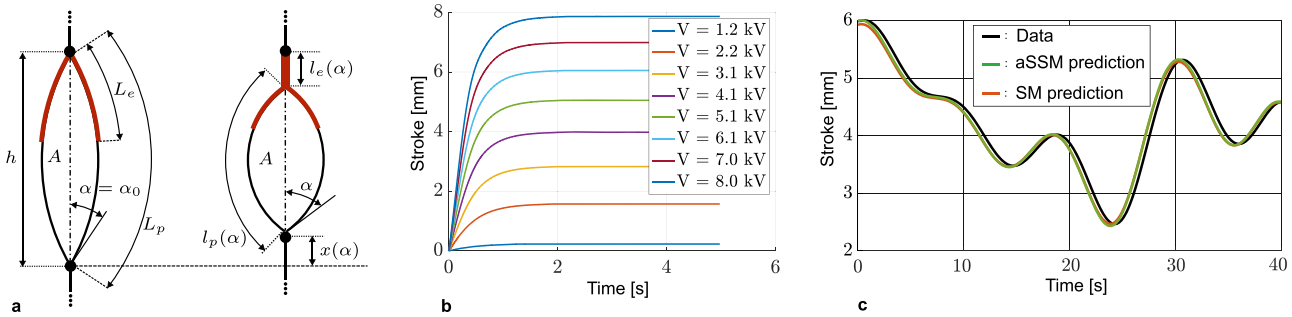


Fig. 5 | Analytical HASEL actuator model and data-driven predictions. **a** Geometry of a single HASEL pouch actuator in the inactive state (left) and actuated state (right). Red segments indicate the electrode-covered (zipped) portion of the shell and black segments the flexible pouch; L_p and L_e denote the pouch and electrode lengths, $l_p(\alpha)$ and $l_e(\alpha)$ the unzipped and zipped lengths, α the pouch opening angle (equal to α_0 at rest), A the constant cross-sectional area of the enclosed fluid, h the initial actuator length, and $x(\alpha)$ the resulting stroke. Adapted from ref. 33. **b** Autonomous response of the analytic HASEL actuator model (13) under different constant voltage levels. **c** Predictions of the data-driven aSSM-based and SM-based models for the actuator stroke in system (13) under random excitation.

shape composed of two intersecting circular segments with central angle $2\alpha_0$ and arc length equal to the undeformed pouch length L_p. The volume of fluid determines the cross-sectional area A, which is related to the angle α through:

$$A = \frac{1}{2}L_p^2\left(\frac{\alpha - \sin\alpha\cos\alpha}{\alpha^2}\right). \tag{11}$$

The initial actuator length is given by:

$$h = L_p\left(\frac{\sin\alpha_0}{\alpha_0}\right). \tag{12}$$

Electrodes of length L_e and width w are attached to the top surface of the actuator on both sides. When the voltage u is applied, the electrodes zip together over a length l_e, starting from the edge of the pouch. If we neglect the thickness contribution from the dielectric fluid, the electrode separation becomes $2t$. Since the membrane is inextensible and the dielectric fluid is incompressible, the geometric parameters L_p, w, and A remain constant throughout the actuation, leading to a vertical contraction of the actuator. During this process, the fluid-filled region retains the cylindrical segment shape, parametrized by the central angle α.

It is possible to relate the arc length of the unzipped portion of the pouch l_p, the zipped length l_e, the stroke of the actuator x, and the capacitance of the zipped region C to the angular deflection α (see Supplementary Material). The model also incorporates a threshold voltage, below which the electrostatic force is insufficient to induce any zipping. Furthermore, it is assumed that the electrical energy arises solely from the region where the electrodes are zipped together, since the electric field in the unzipped region decays rapidly.

In terms of the stroke x_i and the charge Q_i on the zipped region of the electrodes of the i-th pouch, the governing equations read

$$\begin{aligned} m\ddot{x}_i + c\dot{x}_i + kx_i &= mg - \tfrac{1}{2}\tfrac{Q_i^2 C_{x_i}}{C(x_i)^2}, \quad i = 1, \ldots, N \\ \dot{Q}_i &= -\tfrac{1}{RC(x_i)}Q_i + \tfrac{1}{R}u, \end{aligned} \tag{13}$$

describes the dependence of the capacitance on the actuator's stroke. The parameters of the model are tuned to mimic the behavior of the experimental HASEL actuator.

Each pouch is described by Eq. (13), which corresponds to three first-order ordinary differential equations, so the phase-space dimension of the entire actuator is $n = 3N$. The dimension of the external forcing (voltage) is $f = 1$. Given that the actuator exhibits overdamped behavior (see Fig. 5b) and the dynamics of the charge on the electrodes evolve much faster, the reduced-order model is effectively one-dimensional. The single observable used for data-driven modeling is the total stroke of the actuator. Figure 5c presents a comparison between the predictions of the aSSM-based and SM-based reduced-order models under random forcing with $\rho = 0.13$. The models yield normalized mean trajectory errors of $\text{NMTE}_{\text{aSSM}} = 1.7\%$ and $\text{NMTE}_{\text{SM}} = 1.8\%$, respectively. These results confirm the accuracy of data-driven aSSM and SM models for system (13).

Data-driven modeling of experimental artificial muscles

We now consider the experimental HASEL actuator shown in Fig. 6a, which consists of fifteen pouches. Each pouch uses a thermoplastic biaxially oriented polyethylene terephthalate (BoPET) shell filled with dielectric oil; the antagonistic joint of Fig. 6c (see Supplementary Video 2) uses actuators of the same construction. Experimental results under random voltage forcing reveal that the actuator's intrinsic dynamics are significantly faster than the typical rates of change of the inputs necessary for producing typical HASEL contraction patterns arising in practice. This pronounced time-scale separation justifies the use of a one-dimensional reduced-order model based on a slow manifold, given that the input $u(t)$ is one-dimensional.

To build such a model, we use the stroke of the actuator as a single observable and train an SM-based reduced model directly from forced data. The SM is approximated by a polynomial function trained on seven randomly forced trajectories. Notably, a linear approximation

$$x_e(u) = 1.12 \cdot 10^{-7} + 1.56 \cdot 10^{-3}u, \tag{14}$$

proves remarkably effective for this system. For comparison, we also construct an aSSM-based model using a cubic-order approximation for both the manifold parametrization and the reduced dynamics. As shown in Fig. 6b, the prediction from the aSSM model rapidly converges to that of the SM model, offering marginal improvement. This demonstrates that the simpler SM approach, trained solely on forced trajectories, can achieve essentially the same predictive performance without requiring transient decay experiments (see Supplementary Video 3). This behavior remains consistent across voltage inputs with different slowness measure ρ. The example shown in Fig. 6b features the dimensionless rate $\rho = 0.28$, yielding normalized mean trajectory errors of $\text{NMTE}_{\text{aSSM}} = 7.90\%$ and $\text{NMTE}_{\text{SM}} = 8.16\%$. As shown in the figure, both errors fall within the range of experimental uncertainty, estimated from repeated trials using the same voltage inputs.

The construction of the aSSM model, as discussed in Kaundinya et al.[20], requires generating a set of initial conditions as perturbations

https://doi.org/10.1038/s41467-026-77664-0

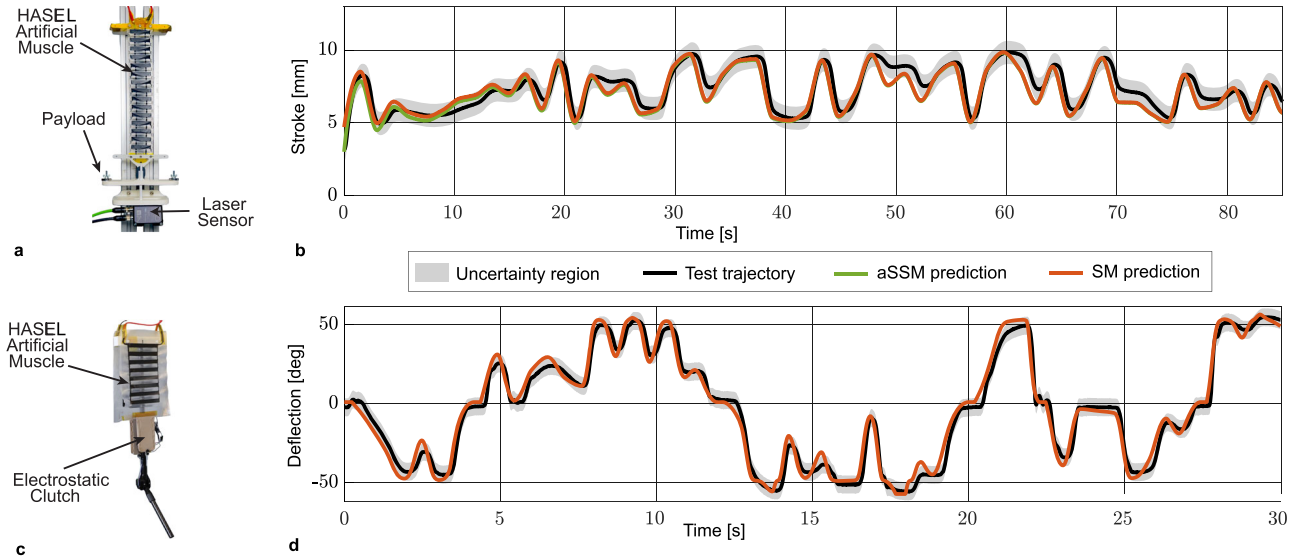


Fig. 6 | Experimental HASEL artificial muscles and data-driven slow manifold predictions. a Single HASEL actuator with payload and laser displacement sensor. **b** Predictions of the actuator stroke under random forcing: the aSSM-based prediction (green) quickly converges to the SM-based prediction (orange), both closely matching the test trajectory (black); the shaded region indicates the uncertainty region estimated from repeated HASEL actuator characterization trials. **c** Musculoskeletal joint with an antagonistic pair of HASEL actuators and electrostatic clutches. **d** Slow-manifold prediction of the joint deflection under random excitation, demonstrating accurate tracking of the test trajectory; the shaded region shows the corresponding angular uncertainty converted using the 4 mm moment arm.

from steady states corresponding to different constant voltages. For a HASEL actuator, these new initial conditions are produced by applying sudden voltage jumps relative to the constant input. Such high-amplitude jumps, however, often trigger hysteretic actuator behavior that would otherwise not arise under typical operating conditions. This mismatch limits the applicability of the aSSM approach based on experimental data for this class of systems.

In contrast, the SM-based reduced modeling relies solely on forced response data, which can be collected under normal operating conditions without introducing unwanted hysteresis. This practical advantage, combined with the comparable prediction accuracy of the SM model, makes the slow manifold approach more suitable for modeling HASEL actuators. Further details on the actuator's hysteresis, as well as on data collection and processing, can be found in the Supplementary Material.

We now extend our analysis from a single actuator to a complete artificial muscle system. Specifically, we investigate an antagonistic configuration composed of two HASEL actuators arranged on opposite sides of a rigid structure, each paired with an electrostatic clutch. This setup, inspired by the design presented by Kazemipour et al.[32] and shown in Fig. 6c, enables an extended range of motion and allows the artificial muscle to emulate the antagonistic actuation of biological limbs. The present hardware is a modified implementation of the same antagonistic HASEL–clutch architecture: the HASEL actuator geometry and link lengths differ from the previous setup, altering the joint kinematics, range of motion, and voltage–angle relation, while the clutch geometry mainly changes the operating voltage and holding margin because the clutch is used here as a binary engagement element. The slow-manifold map and controller are therefore identified and validated on the present setup.

In this configuration, the system features four control inputs: two for activating the HASELs and two for engaging the electrostatic clutches. In the present work, we assume that the HASEL and clutch on a given side are activated simultaneously, and that only one side of the muscle is active at a time. This assumption reduces the input space to a single scalar input: the sign of this input determines which side of the muscle is engaged, thus preserving the antagonistic actuation behavior in a simplified representation. This scalar-input representation specializes the antagonistic joint to position tracking under alternating actuation; co-contraction commands for joint-impedance modulation are discussed as a future extension in the "Discussion".

Unlike isolated actuators, designing decaying trajectories for artificial muscles is more challenging due to the complexity of the multi-input configuration and the mechanical coupling, which introduces friction at the joint. This makes the use of aSSMs less practical, as their construction relies on transient data following step inputs (see Supplementary Section 2), which induces undesirable hysteretic behavior that is atypical under normal operating conditions. In contrast, the SM-based approach demonstrates its practicality by requiring only forced trajectories for training. In this case, we employ a polynomial approximation of the slow manifold up to 7th order, trained using just three forced-response trajectories. As shown in Fig. 6d, the SM-based model accurately predicts the muscle deflection with slowness measure $\rho = 0.22$, yielding a normalized mean trajectory error of $\mathrm{NMTE}_{\mathrm{SM}} = 8.13\%$.

Having validated the predictive accuracy of the data-driven slow manifold models, we now demonstrate their utility for real-time control by implementing model-based feedforward on the antagonistic joint and comparing performance against PI-only and feedforward-only baselines.

SSM-enabled closed-loop control of an antagonistic joint

In order to test our data-driven SM-model in a closed-loop control setting, we observe a time-varying joint angle $\theta_d(t)$ using the antagonistic HASEL–clutch setup of Fig. 6c, with measurement $\theta(t)$. We evaluate three control strategies: proportional-integral (PI) feedback, an inverse-SSM feedforward term added to PI, and inverse-SSM feedforward alone; the corresponding control architectures are summarized in Fig. 7. The PI law is $u(t) = k_p e(t) + k_i \int_0^t e(\tau)\,\mathrm{d}\tau$ with $e(t) = \theta_d(t) - \theta(t)$. The inverse-SSM term is obtained from the identified slow-manifold map $\theta \approx g(u)$ (Section "Data-driven modeling of experimental artificial muscles") via $g^{-1}(\theta_d(t))$.

The gains (k_p, k_i) are tuned separately for the combined and PI-only controllers on a short calibration trajectory and then held fixed.

https://doi.org/10.1038/s41467-026-77664-0

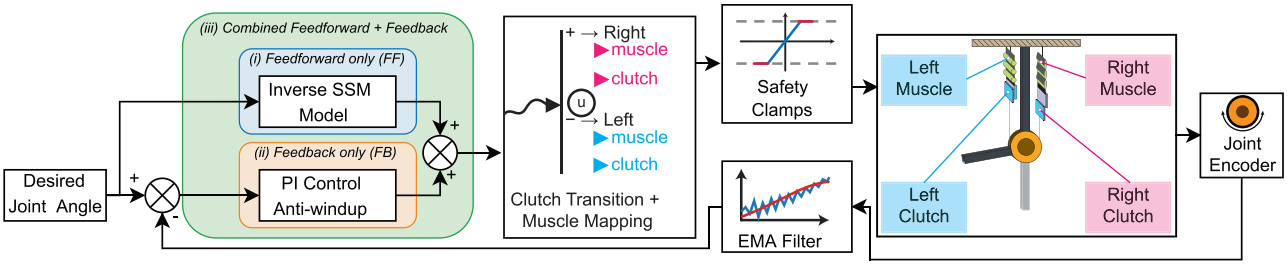


Fig. 7 | Open- and closed-loop control architectures. (i) Feedforward: the desired joint angle is mapped to a voltage command by the inverse SSM model g^{-1}. (ii) Feedback: a proportional–integral (PI) controller with anti-windup acts on the exponential moving average (EMA)-filtered joint-encoder measurement. (iii) Combined controller: feedforward and feedback are summed and routed through the clutch-transition and muscle-mapping stage; safety clamps then enforce saturation and slew-rate limits before driving the antagonistic left/right muscles and their clutches.

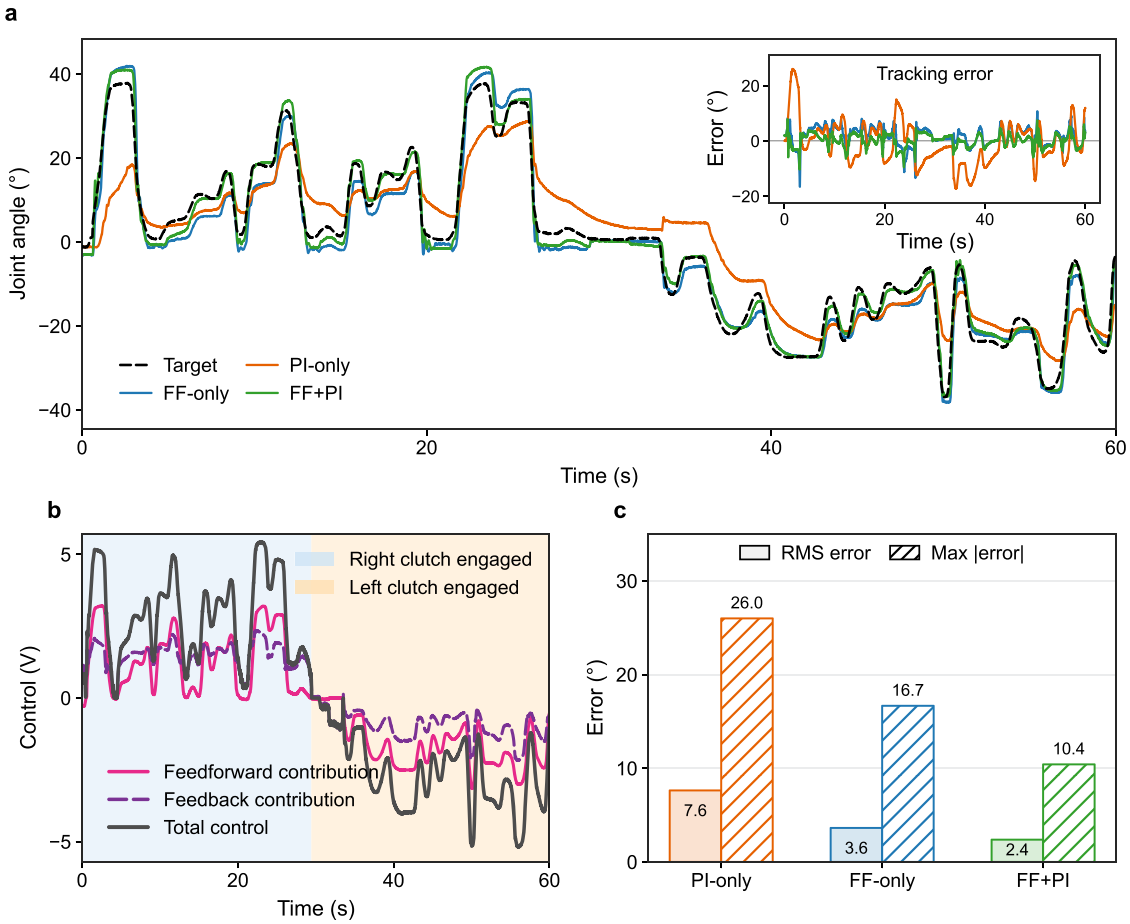


Fig. 8 | Combined model-based feedforward and feedback control achieves superior tracking performance. a Target joint angle (dashed) and measured angle for three controllers: proportional–integral feedback only (PI-only), inverse-SSM feedforward only (FF-only), and combined feedforward plus feedback (FF+PI). **b** Control signal for the FF+PI controller, decomposed into feedforward and feedback contributions; shaded bands indicate engagement of the right and left clutches. **c** Performance summary showing root-mean-square (RMS) error and maximum absolute error $|e|_{\max}$, demonstrating two-thirds error reduction relative to PI-only control.

The selected gains are $(k_p, k_i) = (0.08, 0.12)$ for PI-only and (0.04, 0.12) for the combined controller. All controllers are then evaluated on the same randomized test reference trajectory under identical safety constraints and clutch scheduling. Performance is quantified by the root-mean-square (RMS) tracking error and the maximum absolute error, $\max_t |e(t)|$.

On the unseen trajectory, the inverse-SSM+PI controller achieved the lowest error (RMS 2.38°; max 10.41°). Feedforward-only attained RMS 3.63° and max 16.67°, while PI-only produced RMS 7.63° and max 26.00°. The test trajectory features a slowness measure of $\rho = 0.15$. The control effort, quantified directly from the commanded voltages to the two muscles ($|u_{\text{right}}| + |u_{\text{left}}|$ per sample), was comparable across conditions in RMS and mean magnitude (mean ≈ 2.68–2.98 V; RMS ≈ 3.01–3.15 V), with PI-only exhibiting the largest mean magnitude (2.98 V). Figure 8a overlays the target and the measured angles for all conditions (see also Supplementary Video 4); Fig. 8b decomposes the combined control into feedforward and feedback contributions with shaded clutch engagement. This

also suggests that the residual hysteretic effects, while small, are effectively handled by the feedback controller. Figure 8c summarizes the RMS and maximum absolute errors.

When used alone, the inverse-SSM control strategy tracks the slow trend but cannot reject disturbances, leading to higher peaks in $|e|$. The PI-only strategy corrects errors but requires larger voltages and exhibits slower transients when the antagonistic side switches. In the combined control strategy, the commanded-voltage contributions confirm that feedforward dominates effort: the feedforward term has mean magnitude 1.47 V (RMS 1.77 V) versus 1.21 V (RMS 1.32 V) for the feedback term, i.e., a $\approx 1.22\ \times$ larger mean and $\approx 1.34\ \times$ larger RMS contribution.

We provide additional repeatability and trajectory-generalization analyses on the same physical setup in Supplementary Fig. 3 and Supplementary Table 1.

Taken together, these observations indicate that the SSM-based feedforward supplies the dominant actuation burden, while the PI term effectively rejects disturbances and residual model error.

Discussion

We presented a data-driven reduced-order modeling methodology for artificial muscles and demonstrated its performance on closed-loop control of an antagonistic HASEL-clutch joint. The central observation across our simulations and experiments is a pronounced time-scale separation required for aSSM-based model reduction: trajectories collapse rapidly onto an attracting, low-dimensional set before evolving along a slowly varying response. In this regime, a slow-manifold (SM) model learned directly from forced data suffices for prediction and control, while a full aSSM reduction provides additional accuracy. The latter, however, offers modest additional benefit in practice because it requires fast decay experiments that can excite hysteresis. The advantage of using the reduction on the aSSM instead of the SM would become more evident under milder time-scale separation, for instance, when the forcing varies more rapidly or in soft robots exhibiting slower internal dynamics.

Importantly, the data-driven approach modeling itself is our main contribution: the SM/aSSM workflow developed here is sample-efficient (trained from a handful of forced trajectories), predictive (single-digit NMTE on both single-actuator and antagonistic-muscle tests), and computationally light. It also yields an explicit inverse map g^{-1} with microsecond-level evaluation, enabling real-time feedforward on embedded hardware.

A key outcome of this work is demonstrating that data-driven reduced-order models are not merely accurate predictors but also effective control tools for antagonistic artificial muscle systems. Antagonistic actuation, inspired by biological muscle pairs, offers variable impedance and bidirectional motion, yet controlling such assemblies has remained challenging due to switching dynamics, multi-physics coupling, and the need for real-time computation. By successfully implementing model-based feedforward control on an antagonistic HASEL-clutch joint and achieving substantial error reduction over PI-only baselines, we establish that the learned slow-manifold inverse provides a practical path to precise soft-robot control without prohibitive computational overhead. This bridges a critical gap between theoretical model reduction and deployable robotic systems, showing that bio-inspired antagonistic designs can be controlled accurately using computationally lean, experiment-derived models.

Our control experiments have substantiated these modeling choices. Using the learned inverse map g^{-1} as feedforward and a lightweight PI feedback term, the combined controller achieves the lowest tracking error on an unseen randomized trajectory (Fig. 8). Relative to feedforward-only and PI-only, the RMS error decreases by roughly one-third and two-thirds, respectively, while the maximum absolute error improves accordingly. Notably, the commanded voltage magnitudes delivered to the muscles are of similar scale across all three conditions, indicating that accuracy gains are not obtained by substantially increasing actuation. Within the combined controller, the decomposition of the command shows that the feedforward contribution accounts for the larger share of the effort (mean magnitude ≈ 1.47 V vs. ≈ 1.21 V for feedback), with a comparable dominance in RMS. Thus, the model supplies most of the actuation burden, and the feedback primarily rejects disturbances and residual modeling error.

These findings suggest a practical recipe for soft-robotic muscle control under slowly varying motion goals: (1) learn a one-dimensional slow-manifold map from operational data; (2) use its inverse as a fast, robust feedforward term; and (3) add a small PI loop with anti-windup for robustness. The resulting controller is simple to tune, executes at kHz rates, and remains compatible with antagonistic actuation and clutch scheduling.

The demonstrated approach may also be relevant beyond HASEL actuators. Other soft robotic systems, such as pneumatic artificial muscles (PAMs), dielectric elastomer actuators (DEAs), or shape-memory alloy (SMA) actuators, can exhibit internal transients that are fast relative to the commanded motion. When such time-scale separation is experimentally verified, the proposed workflow may provide a sample-efficient route to reduced-order modeling.

The ability to learn accurate models from a handful of training trajectories makes this practical for field deployment, where extensive data collection is infeasible, opening pathways for adaptive prosthetics, minimally invasive surgical robotics, and collaborative manufacturing where soft, precise actuation is essential. Moreover, the computationally lean nature of the inverse slow-manifold map enables deployment on resource-constrained embedded controllers typical of wearable and portable robotic systems. Recent soft-robotics reviews similarly identify accurate but tractable modeling, control of nonlinear compliant dynamics, and deployment robustness as central barriers for fielded soft robotic systems[3,5,6].

Our approach is not without limitations. The SM approximation presumes slow external variation (small slowness rate ρ), and its fidelity degrades under abrupt voltage changes that elicit hysteresis. Our antagonistic realization assumes mutually exclusive clutch engagement; richer behaviors (e.g., brief overlap or bilateral actuation) will require higher-dimensional slow manifolds. This scalar-input specialization restricts the controller to alternating-actuation position tracking. Tasks requiring bilateral co-contraction, such as independent stiffness or impedance modulation[42–44], bidirectional load holding, disturbance rejection, or preload during rapid reversals, would require a higher-dimensional SM map with independent left/right actuator and clutch inputs.

Finally, while the present inverse map is static, mild rate-dependence could further improve accuracy under faster references. The learned map g should be interpreted as a device-specific calibration of the tested antagonistic joint. Hardware and payload changes or long-term aging can shift the voltage–angle relation; in practice, the PI term compensates moderate mismatch, while persistent increases in tracking error or feedback effort indicate the need for recalibration.

Beyond gradual drift, failure modes separate into controller-level limits and hardware faults. The safety layers described in Methods keep commands within the configured operating envelope, so out-of-range references or violations of the slow-input assumption lead to degraded tracking or saturation rather than unbounded command growth. Hardware faults, such as HASEL dielectric breakdown or loss of clutch engagement, fall outside the controller's corrective authority and would require actuator replacement or fault detection, for example, through voltage/current monitoring or clutch slip sensing.

Based on these limitations, future work will target (1) asynchronous HASEL/clutch activation and simultaneous bilateral actuation

via higher-dimensional aSSMs/SMs, enabling tunable joint stiffness for impedance-modulated tasks; (2) hysteresis-aware or rate-dependent corrections for faster inputs; (3) online adaptation of g to compensate drift; (4) principled optimization of clutch timing to balance performance and safety; and (5) in-loop fault detection for HASEL dielectric breakdown and clutch slip to enable safe field deployment.

Methods

Data-driven modeling via adiabatic spectral submanifolds

For $\epsilon = 0$, we assume that the system (4) has a $\boldsymbol{u}$-dependent, uniformly bounded, and uniformly hyperbolic fixed point $\boldsymbol{x}_0(\boldsymbol{u})$, as explained in Haller and Kaundinya[17]. In this setting, the system has an f-dimensional, normally attracting invariant manifold

$$\mathcal{L}_0 = \left\{(\boldsymbol{x},\boldsymbol{u}) \in \mathbb{R}^n \times \mathbb{R}^f : \boldsymbol{x} = \boldsymbol{x}_0(\boldsymbol{u})\right\}, \tag{15}$$

which is the collection of the $\boldsymbol{x}_0(\boldsymbol{u})$ fixed points and is called critical manifold in the terminology of the geometric singular perturbation theory[39]. The manifold $\mathcal{L}_0$ then satisfies

$$\boldsymbol{A}\boldsymbol{x}_0(\boldsymbol{u}) + \boldsymbol{f}_0(\boldsymbol{x}_0(\boldsymbol{u})) + \boldsymbol{f}_1(\boldsymbol{x}_0(\boldsymbol{u}),\boldsymbol{u}) = \boldsymbol{0}. \tag{16}$$

We now perform a change of variables

$$\boldsymbol{\xi} = \boldsymbol{x} - \boldsymbol{x}_0(\boldsymbol{u}), \tag{17}$$

which flattens out the critical manifold. We can then rewrite Eq. (4)

$$\begin{cases} \dot{\boldsymbol{\xi}} = \boldsymbol{A}(\boldsymbol{x}_0(\boldsymbol{u}) + \boldsymbol{\xi}) + \boldsymbol{f}_0(\boldsymbol{x}_0(\boldsymbol{u}) + \boldsymbol{\xi}) \\ \qquad\quad + \boldsymbol{f}_1(\boldsymbol{x}_0(\boldsymbol{u}) + \boldsymbol{\xi},\boldsymbol{u}) - \boldsymbol{D}_{\boldsymbol{u}}\boldsymbol{x}_0(\boldsymbol{u})\dot{\boldsymbol{u}}, \\ \dot{\boldsymbol{u}} = \epsilon \boldsymbol{w}(\boldsymbol{x}_0(\boldsymbol{u}) + \boldsymbol{\xi}, \epsilon t). \end{cases} \tag{18}$$

We now expand in Taylor series the right-end-side of the first equation in (18) to obtain

$$\begin{aligned} \boldsymbol{f}_0(\boldsymbol{x}_0(\boldsymbol{u}) + \boldsymbol{\xi}) = &\boldsymbol{f}_0(\boldsymbol{x}_0(\boldsymbol{u})) + \boldsymbol{D}_{\boldsymbol{x}}\boldsymbol{f}_0(\boldsymbol{x}_0(\boldsymbol{u}))\boldsymbol{\xi} \\ &+ \frac{1}{2}\boldsymbol{\xi}^{\mathrm{T}}\boldsymbol{D}_{\boldsymbol{x}}^2\boldsymbol{f}_0(\boldsymbol{x}_0(\boldsymbol{u}))\boldsymbol{\xi} + \mathcal{O}(3), \end{aligned} \tag{19}$$

and

$$\begin{aligned} \boldsymbol{f}_1(\boldsymbol{x}_0(\boldsymbol{u}) + \boldsymbol{\xi},\boldsymbol{u}) = &\boldsymbol{f}_1(\boldsymbol{x}_0(\boldsymbol{u}),\boldsymbol{u}) + \boldsymbol{D}_{\boldsymbol{x}}\boldsymbol{f}_0(\boldsymbol{x}_0(\boldsymbol{u}),\boldsymbol{u})\boldsymbol{\xi} \\ &+ \frac{1}{2}\boldsymbol{\xi}^{\mathrm{T}}\boldsymbol{D}_{\boldsymbol{x}}^2\boldsymbol{f}_1(\boldsymbol{x}_0(\boldsymbol{u}),\boldsymbol{u})\boldsymbol{\xi} + \mathcal{O}(3). \end{aligned} \tag{20}$$

Equation (18) thus becomes

$$\begin{cases} \dot{\boldsymbol{\xi}} = \hat{\boldsymbol{A}}(\boldsymbol{u})\boldsymbol{\xi} - \boldsymbol{D}_{\boldsymbol{u}}\boldsymbol{x}_0(\boldsymbol{u})\dot{\boldsymbol{u}} + \frac{1}{2}\boldsymbol{\xi}^{\mathrm{T}}\{\boldsymbol{D}_{\boldsymbol{x}}\boldsymbol{f}_0(\boldsymbol{x}_0(\boldsymbol{u})) \\ \qquad\quad + \boldsymbol{D}_{\boldsymbol{x}}^2\boldsymbol{f}_1(\boldsymbol{x}_0(\boldsymbol{u}),\boldsymbol{u})\}\boldsymbol{\xi} + \mathcal{O}(3), \\ \dot{\boldsymbol{u}} = \epsilon \boldsymbol{w}(\boldsymbol{x}_0(\boldsymbol{u}) + \boldsymbol{\xi}, \epsilon t), \end{cases} \tag{21}$$

with the linear part

$$\hat{\boldsymbol{A}}(\boldsymbol{u}) = \boldsymbol{A} + \boldsymbol{D}_{\boldsymbol{x}}\boldsymbol{f}_0(\boldsymbol{x}_0(\boldsymbol{u})) + \boldsymbol{D}_{\boldsymbol{x}}\boldsymbol{f}_1(\boldsymbol{x}_0(\boldsymbol{u}),\boldsymbol{u}) \in \mathbb{R}^{n\times n}.$$

We will denote by $\boldsymbol{P}(\boldsymbol{u}) \in \mathbb{R}^{n\times n}$ the column matrix of the right eigenvectors of $\hat{\boldsymbol{A}}(\boldsymbol{u})$ and $\boldsymbol{Q}_{\boldsymbol{u}}(\boldsymbol{u}) \in \mathbb{R}^{d\times n}$ the row matrix of the first d left eigenvectors.

We now apply a modal coordinate transformation

$$\boldsymbol{\xi} = \boldsymbol{P}(\boldsymbol{u})\begin{pmatrix}\boldsymbol{\eta}\\ \boldsymbol{v}\end{pmatrix}, \quad \boldsymbol{\eta} \in \mathbb{R}^d, \quad \boldsymbol{v} \in \mathbb{R}^{n-d}. \tag{22}$$

The leading-order approximation of the reduced dynamics on the adiabatic SSM then becomes

$$\begin{aligned} \dot{\boldsymbol{\eta}} = &\boldsymbol{Q}_{\boldsymbol{u}}\hat{\boldsymbol{A}}(\boldsymbol{u})\boldsymbol{P}(\boldsymbol{u})\begin{pmatrix}\boldsymbol{\eta}\\ \boldsymbol{h}_0(\boldsymbol{\eta},\boldsymbol{x}_0(\boldsymbol{u}))\end{pmatrix} \\ &+ \frac{1}{2}\begin{pmatrix}\boldsymbol{\eta}\\ \boldsymbol{h}_0(\boldsymbol{\eta},\boldsymbol{x}_0(\boldsymbol{u}))\end{pmatrix}^{\mathrm{T}}\boldsymbol{P}(\boldsymbol{u})^{\mathrm{T}}(\boldsymbol{D}_{\boldsymbol{x}}\boldsymbol{f}_0(\boldsymbol{x}_0(\boldsymbol{u})) \\ &+ \boldsymbol{D}_{\boldsymbol{x}}^2\boldsymbol{f}_1(\boldsymbol{x}_0(\boldsymbol{u}),\boldsymbol{u}))\boldsymbol{P}(\boldsymbol{u})\begin{pmatrix}\boldsymbol{\eta}\\ \boldsymbol{h}_0(\boldsymbol{\eta},\boldsymbol{x}_0(\boldsymbol{u}))\end{pmatrix} + \mathcal{O}(3), \end{aligned} \tag{23}$$

where the relationship $\boldsymbol{v} = \boldsymbol{h}_0(\boldsymbol{\eta},\boldsymbol{x}_0(\boldsymbol{u}))$ is the leading-order approximation in ϵ of the aSSM parametrization. For a discussion on higher-order corrections, see Haller and Kaundinya[17].

Given a scalar observable $s(t) \in \mathbb{R}^N$, such as the stroke of the HASEL actuator or the deflection angle of the musculoskeletal joint, we apply delay embedding to ensure that the embedding dimension is sufficient to reconstruct the manifold in the observable space[45]. The following procedure enables us to recover the leading-order approximation of the aSSM and its associated reduced dynamics for a scalar external input $u \in \mathbb{R}$:

(1) Given the observed data $s \in \mathbb{R}^N$ at the frozen time limit $u = \bar{u} \in \mathbb{R}$, assess the steady solution $s_0(\bar{u})$.
(2) Delay embed the data and construct $\boldsymbol{x}(t)$ and $\boldsymbol{x}_0(\bar{u})$, with $\boldsymbol{x}, \boldsymbol{x}_0(\bar{u}) \in \mathbb{R}^{p\times N}$.
(3) Define the shift $\boldsymbol{\xi} = \boldsymbol{x} - \boldsymbol{x}_0(\bar{u})$ with respect to the fixed point $\boldsymbol{x}_0(\bar{u})$.
(4) Approximate the tangent space $\boldsymbol{V} \in \mathbb{R}^{p\times d}$ of $\boldsymbol{\xi}(t)$ via singular value decomposition (SVD), where d is the dimension of the reduced-order model. In our case, $d = 1$.
(5) Define the reduced coordinates $\boldsymbol{\eta} = \boldsymbol{V}^{\mathrm{T}}\boldsymbol{x}$, $\boldsymbol{\eta} \in \mathbb{R}^{d\times N}$.
(6) Compute the SSM parametrization $\boldsymbol{\xi} = \boldsymbol{h}_0(\boldsymbol{\eta};\bar{u}) = [\boldsymbol{H}_1(\bar{u}), \ldots \boldsymbol{H}_m(\bar{u})]\boldsymbol{\eta}^{1:m}$, which is a multivariate polynomial and $\boldsymbol{H}_i \in \mathbb{R}^{p\times d_i}$ and it is the zeroth-order approximation in ϵ of the aSSM at $u = \bar{u}$.
(7) Compute the reduced dynamics $\dot{\boldsymbol{\eta}} = \boldsymbol{r}(\boldsymbol{\eta};\bar{u}) = [\boldsymbol{R}_1(\bar{u}), \ldots, \boldsymbol{R}_r(\bar{u})]\boldsymbol{\eta}^{1:r}$, which is again a multivariate polynomial, where $\boldsymbol{R}_i \in \mathbb{R}^{d\times d_i}$ and it is an approximation of Eq. (23) up to the r^{th} order in the reduced coordinate $\boldsymbol{\eta}$.
(8) Compute the SSM parametrization as:

$$\boldsymbol{\xi} = \boldsymbol{h}_0(\boldsymbol{\eta};\bar{u}) = \sum_{|\boldsymbol{k}|=1}^{m} \boldsymbol{H}_{\boldsymbol{k}}(\bar{u})\,\boldsymbol{\eta}^{\boldsymbol{k}}, \tag{24}$$

where $\boldsymbol{H}_{\boldsymbol{k}}(\bar{u}) \in \mathbb{R}^{p\times d_{\boldsymbol{k}}}$ are coefficient matrices, $\boldsymbol{k} = (k_1, \ldots, k_d) \in \mathbb{N}^d$ is a multi-index, $|\boldsymbol{k}| = k_1 + \cdots + k_d$ denotes its total degree, and $\boldsymbol{\eta}^{\boldsymbol{k}} = \eta_1^{k_1}\eta_2^{k_2}\cdots\eta_d^{k_d}$. This expression represents a multivariate polynomial corresponding to the zeroth-order approximation in ϵ of the aSSM evaluated at $u = \bar{u}$.
(9) Compute the reduced dynamics as:

$$\dot{\boldsymbol{\eta}} = \boldsymbol{r}(\boldsymbol{\eta};\bar{u}) = \sum_{|\boldsymbol{k}|=1}^{r} \boldsymbol{R}_{\boldsymbol{k}}(\bar{u})\,\boldsymbol{\eta}^{\boldsymbol{k}}, \tag{25}$$

where $\boldsymbol{R}_{\boldsymbol{k}}(\bar{u}) \in \mathbb{R}^{d\times d_{\boldsymbol{k}}}$ are coefficient matrices. This representation provides a multivariate polynomial approximation of Eq. (23) up to order r in the reduced coordinates $\boldsymbol{\eta}$.

This procedure is repeated for each voltage value u in the sampling. The resulting fixed points $\boldsymbol{x}_0(u)$ are then interpolated to reconstruct the geometry of the critical manifold, along with the associated parametrizations and reduced dynamics as functions of the voltage u. This interpolation assumes that the SSM dimension remains constant across the sampled range. While the tangent spaces of the SSM may vary with voltage, one may interpolate them or, to reduce computational cost, assume a constant tangent space. In the latter case, it is

essential to ensure that this fixed plane remains sufficiently transverse to the fast subspace at all voltage values. If the fast subspace is strongly non-normal relative to the slow one, oblique projections may also be employed (see Bettini et al.[16,46]).

Data-driven modeling via slow manifold

For $\epsilon > 0$ small enough, the critical manifold $\mathcal{L}_0$ as defined in Eq. (15) perturbs into a unique, attracting, and f-dimensional slow manifold (SM)

$$\mathcal{L}_0 = \left\{(\boldsymbol{x}, \boldsymbol{u}) \in \mathbb{R}^n \times \mathbb{R}^f : \boldsymbol{x} = \boldsymbol{x}_\epsilon(\boldsymbol{u})\right\}, \tag{26}$$

which is diffeomorphic to $\mathcal{L}_0$. For further details, we refer to Haller and Kaundinya[17].

As observed from experimental data and seen in Fig. 2c, system trajectories rapidly converge not only to the aSSM, but also to the underlying SM under slowly varying external inputs. This observation enables the direct identification of the SM from forced response data, effectively treating it as a mapping from the input into the observable. For a scalar observable $s(t) \in \mathbb{R}$ and a scalar input $u(t) \in \mathbb{R}$, the SM can be approximated as a polynomial function

$$x_\epsilon(u) \doteq s(u) = \sum_{i=0}^{n} S_i u^i, \quad S_i \in \mathbb{R}, \tag{27}$$

where S_i denotes the coefficient of the i-th order term in u. Alternative approximations (radial basis functions, neural networks; see refs. 47–49) could also be used, but have turned out to be less efficient in our tests (see Supplementary Section 2).

Uncertainty-region estimation

The uncertainty region was estimated from repeated HASEL actuator characterization measurements. Displacement responses were compared at uniformly spaced voltage values between 0 and 7 kV, with a spacing of 0.01 kV. At each voltage value, the uncertainty width was defined as the largest difference between the displacement measured during increasing- and decreasing-voltage ramps across the selected trials. The plotted band corresponds to the nominal response ± half of this width. For joint-angle data, displacement uncertainty was converted to angular uncertainty using the 4 mm moment arm.

Control design and implementation

As noted in Section "SSM-enabled closed-loop control of an antagonistic joint", we evaluate three controller realizations for the antagonistically actuated HASEL elbow: (1) feedforward only, (2) PI-only, and (3) combined feedforward+feedback. All three realizations respect identical safety constraints, apply the same actuation timing for the clutched antagonists, and run with a fixed sampling period T_s (1 kHz in our implementation). The overall signal flow is summarized in the control block diagram (Fig. 7), which comprises an inverse SSM-based feedforward path, a PI feedback path with anti-windup operating in the EMA-filtered measurement, a clutch transition and actuator mapping stage, and terminal safety clamps that enforce hardware limits before driving the antagonistic muscles and clutches. In the following, we summarize the control laws, discretization details, and the antagonistic actuation workflow. Let $\theta_d(t)$ denote the desired joint angle and $\theta(t)$ the measured angle. The control signal $V(t)$ is the commanded high-voltage applied to the active muscle. Safety constraints include a voltage saturation $V \in [\underline{V}, \overline{V}]$ and a slew-rate bound $|V(t) - V(t - T_s)| \le \Delta V_{\max}$. In discrete time, the filtered angle $\tilde{\theta}_k$ is obtained by a first-order low-pass on the raw measurement to suppress quantization/noise.

We identify a static, monotone map between voltage and quasi-static joint angle, $\theta \approx g(V)$ (Section "Data-driven modeling of experimental artificial muscles"). The feedforward command inverts this relation at the desired angle trajectory:

$$V_{\mathrm{ff}}(t) = g^{-1}\left(\theta_d(t)\right).$$

We precompute a dense one-dimensional interpolant over $(V, g(V))$ from the learned polynomial forward map and recover V_{ff} by linear interpolation. This avoids per-sample root finding and yields microsecond-level runtime. θ_d is clipped to the calibrated image of g to avoid extrapolation; the resulting V_{ff} is then clipped to $[\underline{V}, \overline{V}]$ and rate-limited by $\Delta V_{\max}$. In the feedforward-only benchmark, the applied command is:

$$V(t) = \mathrm{sat}_{\underline{V}, \overline{V}}(u(t)), \qquad u(t) = \mathrm{rl}_{\Delta V_{\max}}\{V_{\mathrm{ff}}(t)\},$$

where sat enforces voltage bounds set by the HV driver's output range and the HASEL muscle's dielectric breakdown voltage, and $\mathrm{rl}_{\Delta V_{\max}}\{\cdot\}$ is a slew-rate limiter enforcing $|u(t) - u(t - T_s)| \le \Delta V_{\max}$ (sampling period T_s); equivalently $|\dot{u}(t)| \le S_{\max}$ with $S_{\max} = \Delta V_{\max}/T_s$ (V/s). We tune $\Delta V_{\max}$ to limit abrupt command changes that can cause overshoot or disrupt antagonistic clutch scheduling, while respecting hardware slew limits.

We employ a PI controller on the tracking error $e(t) = \theta_d(t) - \theta(t)$:

$$V_{\mathrm{fb}}(t) = k_p\, e(t) + k_i \int_0^t e(\tau)\, \mathrm{d}\tau.$$

Discrete-time realization (sampling T_s) uses trapezoidal integration for the integral state and conditional integration for anti-windup: the integrator is frozen whenever the tentative command would violate saturation or the slew-rate limit. The measurement is low-pass filtered as $\tilde{\theta}_k = \alpha\, \theta_k + (1 - \alpha)\, \tilde{\theta}_{k-1}$ with a small α.

In the PI-only benchmark, the applied command is:

$$V(t) = \mathrm{sat}_{\underline{V}, \overline{V}}\left(\mathrm{rl}_{\Delta V_{\max}}\{V_{\mathrm{fb}}(t)\}\right).$$

The combined controller superposes the two contributions before enforcing identical safety constraints:

$$V_{\mathrm{tot}}(t) = V_{\mathrm{ff}}(t) + V_{\mathrm{fb}}(t), \quad V(t) = \mathrm{sat}_{\underline{V}, \overline{V}}\left(\mathrm{rl}_{\Delta V_{\max}}\{V_{\mathrm{tot}}(t)\}\right).$$

The feedforward term supplies the bulk of the command from the SSM-based model; the PI term compensates residual model error and disturbances.

The elbow is driven by two antagonistic HASEL muscles, each coupled through an on/off clutch. At any time only one clutch is engaged and receives the command $V(t)$. We implement a light-weight state machine to schedule side switching safely and smoothly. A transition is requested when the reference traverses a dead zone around zero effort (e.g., $|V_{\mathrm{ff}}| < \varepsilon$ in feedforward/combined modes) or when the desired angle changes sign in PI-only mode. Upon trigger, both voltages are set to zero, the target clutch is engaged, and we wait a fixed mechanical engagement time τ_{eng}. After engagement, the active-side voltage is ramped linearly from 0 to its target magnitude over τ_{ramp} to avoid impulses. A short cooldown τ_{cool} prevents chatter under dithering references. All safety checks (saturation, slew-rate, digital outputs in {0,1}, and configured joint-angle bounds) are enforced on the final command delivered to hardware.

Each controller variant (feedforward-only, PI-only, combined) tracks the same reference trajectory under the same safety constraints and clutch scheduler. Feedforward-only has no PI gains; for the PI-only and combined conditions, PI gains were tuned separately on a short calibration trajectory, targeting low RMS tracking error with stable operation under the same saturation and slew-rate limits, and were then held fixed for the benchmark trajectory.

Data availability

All data discussed in the results are publicly available on Zenodo at https://doi.org/10.5281/zenodo.21411485, ref. 50.

Code availability

All codes supporting the results presented here are publicly available on Zenodo at https://doi.org/10.5281/zenodo.21411485, ref. 50.

References

1. Rus, D. & Tolley, M. T. Design, fabrication and control of soft robots. *Nature* **521**, 467–475 (2015).
2. Shih, B. et al. Electronic skins and machine learning for intelligent soft robots. *Sci. Robot.* **5**, eaaz9239(2020).
3. Yasa, O. et al. An overview of soft robotics. *Annu. Rev. Control Robot. Auton. Syst.* **6**, 1–29 (2023).
4. Mirvakili, S. M. & Hunter, I. W. Artificial muscles: mechanisms, applications, and challenges. *Adv. Mater.* **30**, 1704407 (2018).
5. Li, M., Pal, A., Aghakhani, A., Peña-Francesch, A. & Sitti, M. Soft actuators for real-world applications. *Nat. Rev. Mater.* **7**, 235–249 (2022).
6. Della Santina, C., Duriez, C. & Rus, D. Model-based control of soft robots: a survey of the state of the art and open challenges. *IEEE Control Syst. Mag.* **43**, 30–65 (2023).
7. Benner, P., Gugercin, S. & Willcox, K. A survey of projection-based model reduction methods for parametric dynamical systems. *SIAM Rev.* **57**, 483–531 (2015).
8. Ghadami, A. & Epureanu, B. I. Data-driven prediction in dynamical systems: recent developments. *Philos. Trans. R. Soc. A* **380**, 20210213 (2022).
9. Haller, G. *Modeling Nonlinear Dynamics from Equations and Data—With Applications to Solids, Fluids, and Controls* (Society for Industrial and Applied Mathematics, 2025).
10. Haller, G. & Ponsioen, S. Nonlinear normal modes and spectral submanifolds: existence, uniqueness and use in model reduction. *Nonlinear Dyn.* **86**, 1493–1534 (2016).
11. Cenedese, M., Axås, J., Bäuerlein, B., Avila, K. & Haller, G. Data-driven modeling and prediction of non-linearizable dynamics via spectral submanifolds. *Nat. Commun.* **13**, 872 (2022).
12. Cenedese, M., Axås, J., Yang, H., Eriten, M. & Haller, G. Data-driven nonlinear model reduction to spectral submanifolds in mechanical systems. *Philos. Trans. R. Soc. A* **380**, 20210194 (2022).
13. Axås, J., Cenedese, M. & Haller, G. Fast data-driven model reduction for nonlinear dynamical systems. *Nonlinear Dyn.* **111**, 7941–7957 (2023).
14. Bettini, L., Cenedese, M. & Haller, G. Model reduction to spectral submanifolds in piecewise smooth dynamical systems. *Int. J. Non-Linear Mech.* **163**, 104753 (2024).
15. Axås, J., Bäuerlein, B., Avila, K. & Haller, G. Data-driven modeling of subharmonic forced response due to nonlinear resonance. *Sci. Rep.* **14**, 25991 (2024).
16. Bettini, L., Kaszás, B., Zybach, B., Dual, J. & Haller, G. Data-driven nonlinear model reduction to spectral submanifolds via oblique projection. *Chaos* **35**, 043135 (2025).
17. Haller, G. & Kaundinya, R. S. Nonlinear model reduction to temporally aperiodic spectral submanifolds. *Chaos* **34**, 043152 (2024).
18. Alora, J., Cenedese, M., Schmerling, E., Haller, G. & Pavone, M. Data-driven spectral submanifold reduction for nonlinear optimal control of high-dimensional robots. In *2023 IEEE International Conference on Robotics and Automation (ICRA)* 2627–2633 (IEEE, 2023).
19. Alora, J. I., Cenedese, M., Haller, G. & Pavone, M. Discovering dominant dynamics for nonlinear continuum robot control. *npj Robot.* **3**, 5 (2025).
20. Kaundinya, R. S. et al. Data-driven soft robot control via adiabatic spectral submanifolds. *Int. J. Robot. Res.* 02783649261461630 (2026).
21. Asano, Y. et al. Human mimetic musculoskeletal humanoid kengoro toward real world physically interactive actions. In *2016 IEEE-RAS 16th International Conference on Humanoid Robots (Humanoids)* 876–883 (IEEE, 2016).
22. Jäntsch, M. et al. Anthrob—a printed anthropomimetic robot. In *2013 13th IEEE-RAS International Conference on Humanoid Robots (Humanoids)* 342–347 (IEEE, 2013).
23. Richter, C. et al. Musculoskeletal robots: scalability in neural control. *IEEE Robot. Autom. Mag.* **23**, 128–137 (2016).
24. Acome, E. et al. Hydraulically amplified self-healing electrostatic actuators with muscle-like performance. *Science* **359**, 61–65 (2018).
25. Yang, G.-Z. et al. Ten robotics technologies of the year. *Sci. Robot.* **4**, eaaw1826 (2019).
26. Buchner, T. J. K. et al. Electrohydraulic musculoskeletal robotic leg for agile, adaptive, yet energy-efficient locomotion. *Nat. Commun.* **15**, 7634 (2024).
27. Gravert, S.-D. et al. Low-voltage electrohydraulic actuators for untethered robotics. *Sci. Adv.* **10**, eadi9319 (2024).
28. Kurumaya, S., Suzumori, K., Nabae, H. & Wakimoto, S. Musculoskeletal lower-limb robot driven by multifilament muscles. *ROBOMECH J.* **3**, 18 (2016).
29. Niiyama, R., Nagakubo, A. & Kuniyoshi, Y. Mowgli: a bipedal jumping and landing robot with an artificial musculoskeletal system. In *2007 IEEE International Conference on Robotics and Automation (ICRA)* 2546–2551 (IEEE, 2007).
30. Niiyama, R., Nishikawa, S. & Kuniyoshi, Y. Athlete robot with applied human muscle activation patterns for bipedal running. In *2010 10th IEEE-RAS International Conference on Humanoid Robots, Humanoids* (IEEE, 2010).
31. Ogawa, K., Narioka, K. & Hosoda, K. Development of whole-body humanoid "pneumat-bs" with pneumatic musculoskeletal system. In *2011 IEEE/RSJ International Conference on Intelligent Robots and Systems* 4838–4843 (IEEE, 2011).
32. Kazemipour, A., Hinchet, R. & Katzschmann, R. K. Stretchable electrohydraulic artificial muscle for full motion ranges in musculoskeletal antagonistic joints. *arXiv* https://doi.org/10.48550/arXiv.2409.11017 (2024).
33. Kellaris, N., Venkata, V., Rothemund, P. & Keplinger, C. An analytical model for the design of Peano-Hasel actuators with drastically improved performance. *Extrem. Mech. Lett.* **29**, 100449 (2019).
34. Saif, M. T. A., Alaca, B. E. & Sehitoglu, H. Analytical modeling of electrostatic membrane actuator for micro pumps. *J. Microelectromechanical Syst.* **8**, 335–345 (1999).
35. Maffli, L., Rosset, S. & Shea, H. Zipping dielectric elastomer actuators: characterization, design and modeling. *Smart Mater. Struct.* **22**, 104013 (2013).
36. Moretti, G., Duranti, M., Righi, M., Vertechy, R. & Fontana, M. Analysis of dielectric fluid transducers. In *Electroactive Polymer Actuators and Devices (EAPAD) XX*. Proc. SPIE 10594, 105940W (SPIE, 2018).
37. Johnson, B. et al. Identification and control of a nonlinear soft actuator and sensor system. *IEEE Robot. Autom. Lett.* **5**, 3783–3790 (2020).
38. Yeh, Y., Cisneros, N., Wu, Y., Rabenorosoa, K. & Le Gorrec, Y. Modeling and position control of the hasel actuator via port-hamiltonian approach. *IEEE Robot. Autom. Lett.* **7**, 1–8 (2022).
39. Fenichel, N. Geometric singular perturbation theory for ordinary differential equations. *J. Differ. Equ.* **31**, 53–98 (1979).
40. van der Schaft, A. & Jeltsema, D. Port-hamiltonian systems theory: an introductory overview. *Found. Trends Syst. Control* **1**, 173–378 (2014).
41. Lohmayer, M., Kotyczka, P. & Leyendecker, S. Exergetic port-hamiltonian systems: modelling basics. *Math. Comput. Model. Dyn. Syst.* **27**, 489–521 (2021).

42. Hogan, N. Impedance control: an approach to manipulation: part I—theory. *J. Dyn. Syst. Meas. Control* **107**, 1–7 (1985).
43. Vanderborght, B. et al. Variable impedance actuators: a review. *Robot. Auton Syst.* **61**, 1601–1614 (2013).
44. Kazemipour, A. & Katzschmann, R. K. Decoupling torque and stiffness: a unified modeling and control framework for antagonistic artificial muscles. In *2026 IEEE 9th International Conference on Soft Robotics (RoboSoft)* 813–820 (IEEE, 2026).
45. Rand, D. & Young, L.-S. (eds.). *Detecting Strange Attractors in Turbulence* (Springer, 1981).
46. Bettini, L., Kazemipour, A., Katzschmann, R. K. & Haller, G. General oblique projections for model reduction via spectral submanifolds. *Chaos* **36**, 053122 (2026).
47. Powell, M. J. D. *The Theory of Radial Basis Function Approximation in 1990* (Oxford University Press, 1992).
48. Hagan, M., Demuth, H., Beale, M. & De Jesús, O. *Neural Network Design* (Martin Hagan, 2014).
49. Park, J. & Sandberg, I. W. Universal approximation using radial-basis-function networks. *Neural Comput.* **3**, 246–257 (1991).
50. Bettini, L., Kazemipour, A., Katzschmann, R. K. & Haller, G. Matlab code for nonlinear spectral modeling and control of soft-robotic muscles from data. *Zenodo* https://doi.org/10.5281/zenodo.21411485 (2026).

Acknowledgements

We are grateful to Joar Axås for the preliminary investigations he carried out in modeling the HASEL actuator from data. We also thank Patricia Apostol for her contribution to the code used to generate the data for the example in "Illustration of data-driven aSSM and SM modeling on analytic models", and Roshan S. Kaundinya for the valuable discussions on applying adiabatic SSM to control.

Author contributions

L.B., A.K., R.K.K., and G.H. designed the research. L.B. and A.K. carried out the research. L.B. developed the modeling part and developed the related software. A.K. performed the experiments and developed the control part. L.B. and A.K. wrote the paper. R.K.K. and G.H. reviewed the paper. G.H. and R.K.K. led the research team.

Funding

This work was supported by the Swiss National Science Foundation (grant 200021_214908 to G.H. and grant 200021_215489 to R.K.K.); the Swiss State Secretariat for Education, Research and Innovation (to A.K.); and ETH Zurich (grant ETH-17 22-1 to R.K.K.). Open access funding provided by Swiss Federal Institute of Technology Zurich.

Competing interests

The authors declare no competing interests.

Additional information

Supplementary information The online version contains supplementary material available at https://doi.org/10.1038/s41467-026-77664-0.

Correspondence and requests for materials should be addressed to Robert K. Katzschmann or George Haller.

Peer review information *Nature Communications* thanks the anonymous reviewers for their contribution to the peer review of this work. A peer review file is available.

Reprints and permissions information is available at http://www.nature.com/reprints

Publisher's note Springer Nature remains neutral with regard to jurisdictional claims in published maps and institutional affiliations.

Open Access This article is licensed under a Creative Commons Attribution 4.0 International License, which permits use, sharing, adaptation, distribution and reproduction in any medium or format, as long as you give appropriate credit to the original author(s) and the source, provide a link to the Creative Commons licence, and indicate if changes were made. The images or other third party material in this article are included in the article's Creative Commons licence, unless indicated otherwise in a credit line to the material. If material is not included in the article's Creative Commons licence and your intended use is not permitted by statutory regulation or exceeds the permitted use, you will need to obtain permission directly from the copyright holder. To view a copy of this licence, visit http://creativecommons.org/licenses/by/4.0/.

© The Author(s) 2026